PHYSICAL REVIEW B **111**, 195417 (2025)

Material induced bianisotropy of hybrid nanostructures: From a single meta-atom resonance to metasurfaces with trapped modes

Mariia A. Poleva,[1,*] Carsten Rockstuhl,[1,2] and Andrey B. Evlyukhin[3,4,†]
[1]Institute of Theoretical Solid State Physics, Karlsruhe Institute of Technology, Kaiserstrasse 12, 76131 Karlsruhe, Germany
[2]Institute of Nanotechnology, Karlsruhe Institute of Technology, Kaiserstrasse 12, 76131 Karlsruhe, Germany
[3]Institute of Quantum Optics, Leibniz University Hannover, Welfengarten 1, Hannover 30167, Germany
[4]Cluster of Excellence PhoenixD, Leibniz University Hannover, Welfengarten 1A, Hannover 30167, Germany

(Received 11 December 2024; revised 28 February 2025; accepted 28 April 2025; published 13 May 2025)

The optical properties of Janus-type hybrid silicon-gold nanocylinders are theoretically studied. We show that the inhomogeneity of the internal material in these particles causes a strong bianisotropic response. Their lack of inversion symmetry formally determines the bianisotropic response of hybrid nanocylinders. We demonstrate a method for obtaining in advance information on nonzero components of the dipole polarizability tensor of hybrid particles by analyzing the relationship between their symmetry properties and the multipole composition of their eigenmodes. The spectral response of metasurfaces composed of a periodic arrangement of such particles can feature strong resonances associated with multipole coupling and the excitation of quasibound states in the continuum (quasi-BICs). Using the resonant bianisotropic properties of the hybrid particles and the ability to tune the quasi-BICs (trapped modes) to a predetermined wavelength by choosing the metasurface period, we demonstrate the excitation of electric and magnetic types of quasi-BICs in the infrared region. The ability to switch between these types of quasi-BICs by changing the incident light polarization is discussed. We also demonstrate that, unlike purely dielectric metasurfaces, the excitation of the quasi-BICs in hybrid metasurfaces leads to a resonant absorption of light.

DOI: 10.1103/PhysRevB.111.195417

I. INTRODUCTION

For decades, the nanophotonics community has explored plasmonic structures due to their exceptional ability to enhance and confine electromagnetic fields at the subwavelength scale [1–3]. However, the significant absorption observed in noble metals creates many obstacles, which limit the applicability of these nanophotonic devices. Still, the absorbing properties of plasmonic structures are widely exploited to create saturable and perfect absorbers [4–6]. Moreover, such structures demonstrate a high Purcell enhancement due to the excitation of localized surface plasmon polariton resonance [7].

Alternatively, all-dielectric high-index nanoresonators have gained a lot of attention, providing tools for the efficient control of the light-matter interaction [8–10]. Unlike their plasmonic counterparts, dielectric nanoantennes possess minimal absorption because they lack free electrons. Consequently, the quality factor of dielectric nanostructures is less affected by nonradiative losses and is instead primarily limited by radiative damping. At the same time, the dielectric resonators of different shapes sustain magnetic and electric low-order multipolar responses of comparable strength as shown theoretically and experimentally [11–14]. The resonances of dielectric particles , accompanied by a concentration of both electric and magnetic energy on a subwavelength scale [15–17], can be controlled by their shape, size, and material [18–20].

Although dielectric structures have advantages compared to plasmonic ones, using dielectrics reduces the field enhancement and, hence, the Purcell factor, essential for sensing and other applications [21,22]. Hybrid metal-dielectric nanostructures are a viable solution to overcome the limitations of plasmonic and dielectric structures individually. Hybrid nanostructures promise to combine the beneficial properties of metallic nanostructures, such as strong confinement of electromagnetic energy, and dielectric nanostructures, such as high scattering directivity and low losses [21,23]. Hybrid nanostructures, including their periodic arrays (metasurfaces), have already been extensively studied theoretically and experimentally [21,23–28]. The use of hybrid metasurfaces for refractive index sensing with high sensitivity was proposed in Ref. [25]. Reconfigurable hybrid metasurfaces incorporating phase transition material into meta-atoms [26] and hybrid metasurfaces with broken out-of-plane symmetry [29] have been recently proposed for efficient control of light properties. The optical properties of planar waveguides and thin-film solar cells in combination with periodic arrays of metallic nanoparticles were theoretically studied in [30].

---

[*] Contact author: mariia.poleva@kit.edu
[†] Contact author: evlyukhin@iqo.uni-hannover.de

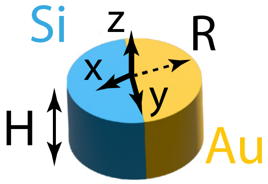

FIG. 1. Schematic illustration of a Janus-type hybrid cylindrical particle composed of silicon and gold and the orientation of the Cartesian coordinate system.

Recently, periodic 2D arrays of dielectric nanoantennas (metasurfaces) have been shown to support the excitation of ultra-narrow high-Q resonances associated with bound states in the continuum (BIC) or, in other words, trapped modes [31–34]. True BIC modes are confined within the structure and cannot be excited from free space. Their Q-factors are limited only by the nonradiative losses, providing perfect confinement of optical energy and making these modes attractive from fundamental and application perspectives [35]. For symmetry-protected BICs [33], the external excitation of high-Q resonances associated with such modes is possible if the symmetry of the unit cell of the array is broken. The BICs are then transformed into quasi-BICs with a large but finite Q-factor [36–38]. The lack of inversion symmetry leads to the appearance of bianisotropic properties of the periodic nanostructure, which opens a radiation channel for the excitation of quasi-BICs [38]. The excitation of quasi-BICs results in high-Q resonant features in the transmission and reflection spectra of metasurfaces and strong near-field enhancement around them [39].

In this theoretical and numerical work, taking into account the great interest in studying metasurfaces of various materials types [40,41], the primary purpose is to explore how collective interactions between hybrid nanoparticles in metasurfaces can affect their collective resonant electromagnetic properties. We investigate the optical properties of a single Janus-type hybrid silicon-gold cylindrical nanoantenna (Fig. 1) and the excitation of the quasi-BIC modes in a 2D array of such particles. We study the possibility of using the material inhomogeneity of hybrid particles with a symmetrical shape to tune the excitation of quasi-BICs in metasurfaces composed of such particles. In this case, special attention is paid to the study of the features of the resonant response of the metasurface caused by the hybrid nature of its constituents, including the distribution and concentration of fields in the unit cell of the metasurface. In the case of hybrid structures, information about the distribution of near electromagnetic fields is of particular importance, as it reveals new possibilities for manipulating light energy on subwavelength scales by combining resonances of the plasmonic and dielectric parts.

Besides this introduction, our paper is structured into three sections. First, we outline the formalism of multipole decomposition of the scattered far field for single antennas and metasurfaces. Second, we show that introducing material inhomogeneities leads to a decrease in antenna symmetry and the appearance of a bianisotropy. Finally, by tuning the period of the metasurfaces to support quasi-BIC at a given wavelength [37], we calculate and analyze the resonant reflectance, transmission, and absorption spectra of the corresponding hybrid metasurfaces for different polarizations of the normally incident waves.

II. THEORETICAL BACKGROUND

In our study, we apply a phenomenological approach in which electromagnetic fields are calculated using Maxwell's equations, and material characteristics (dielectric permittivities) are taken from experimental data [42,43]. To solve Maxwell's equations in the frequency domain, we use COMSOL Multiphysics. Based on the finite element method, the software numerically calculates, depending on illumination conditions, the total electric fields inside and near the considered nanostructures, the radiation pattern, and the total scattered and absorbed powers. For a deeper understanding of the physical causes of the numerical results, we perform a multipole expansion of the scattered field. The following subsections outline the main equations and details of our analytical approach.

A. Multipole response of a single particle

We study the optical properties of a Janus-type hybrid Si-Au nanoparticle schematically presented in Fig. 1. Half of the particle is composed of silicon, and the other half is composed of gold. The nanoparticles are geometrically characterized by a radius R and a height H. The particle's dielectric permittivity ε_{p} can be presented as

$$\varepsilon_{\mathrm{p}}(\mathbf{r},\omega)=\begin{cases}\varepsilon_{\mathrm{Si}}(\omega), & \mathbf{r}\in V_{\mathrm{Si}},\\ \varepsilon_{\mathrm{Au}}(\omega), & \mathbf{r}\in V_{\mathrm{Au}},\end{cases} \tag{1}$$

where $\varepsilon_{\mathrm{Si}}(\omega)$ and $\varepsilon_{\mathrm{Au}}(\omega)$ are the silicon and gold permittivities, respectively, V_{Si} and V_{Au} are the volumes occupied by silicon and gold, respectively (Fig. 1). The total volume of the particle is given my $V_{\mathrm{p}}=V_{\mathrm{Si}}+V_{\mathrm{Au}}$. We consider air as the surrounding medium with a nondispersive relative dielectric function of $\varepsilon_{\mathrm{s}}=1$.

When the particle is illuminated by a linearly polarized plane wave propagating into a direction given by the wave vector $\mathbf{k}$, the total electric field $\mathbf{E}'(\mathbf{r})$ inside the particle is numerically calculated for a fixed angular frequency ω using COMSOL. A time dependence according to $e^{-i\omega t}$ is used throughout the work. We implicitly assume that all field quantities depend on the frequency, and we drop the frequency argument for convenience.

After introducing the induced polarization as $\mathbf{P}(\mathbf{r})=\varepsilon_0(\varepsilon_{\mathrm{p}}(\mathbf{r})-\varepsilon_s)\mathbf{E}'(\mathbf{r})$, the scattered electric field $\mathbf{E}_{\mathrm{sc}}$ in the far-field can be written as (see, for example, [44])

$$\mathbf{E}_{\mathrm{sc}}(\mathbf{r})=\frac{k^2}{\varepsilon_0\varepsilon_s}\int_{V_{\mathrm{p}}}\hat{G}^{\mathrm{FF}}(\mathbf{r},\mathbf{r}')\mathbf{P}(\mathbf{r}')d\mathbf{r}', \tag{2}$$

where ε_0 is the vacuum permittivity, and k is the wave number in the surrounding medium. $\hat{G}^{\mathrm{FF}}(\mathbf{r},\mathbf{r}')$ is the far-field approximation of the underlying Green's tensor $\hat{G}^{\mathrm{FF}}(\mathbf{r},\mathbf{r}')$ of the homogeneous surrounding medium [44] given by

$$\hat{G}^{\mathrm{FF}}(\mathbf{r},\mathbf{r}')=\frac{e^{ikr}}{4\pi r}(\hat{1}-\mathbf{nn})e^{-ik(\mathbf{n}\cdot\mathbf{r}')}, \tag{3}$$

where $\mathbf{nn}$ is the dyadic product of the unit vector $\mathbf{n} = \mathbf{r}/r$ directed to the observation point from the origin of the coordinate system which, in our case, is taken at the geometrical center of the particle. $\hat{1}$ is the 3×3 unit tensor.

Using (3), the scattered field is written as

$$\mathbf{E}_{\rm sc}(\mathbf{r}) = \frac{k^2 e^{ikr}}{4\pi\varepsilon_0\varepsilon_s r}(\hat{1} - \mathbf{nn})\int_{V_{\rm p}} e^{-ik(\mathbf{n}\cdot\mathbf{r}')}\mathbf{P}(\mathbf{r}')d\mathbf{r}'. \quad (4)$$

The factor $e^{-ik(\mathbf{n}\cdot\mathbf{r}')}$ can be expanded using spherical harmonics as [45]

$$e^{-ik(\mathbf{n}\cdot\mathbf{r}')} = 4\pi\sum_{l=0}^{\infty}\sum_{m=-l}^{l}(-i)^l j_l(kr')Y^*_{lm}(\theta,\varphi)Y_{lm}(\theta',\varphi'), \quad (5)$$

where $j_l(kr')$ is the lth order spherical Bessel function, $Y_{lm}(\theta,\varphi)$ is the scalar spherical harmonics, θ and φ (θ' and φ') are the polar and azimuthal angles of $\mathbf{n}$ ($\mathbf{r}'$) in the spherical coordinate system, and the asterisk (*) denotes the complex conjugation. Substituting representation (5) into (4) and using the method from Ref. [44], the scattered electric field can be represented as a superposition of various multipole contributions:

$$\mathbf{E}_{\rm sc}(\mathbf{r}) = \frac{k^2}{\varepsilon_0\varepsilon_s}\frac{e^{ikr}}{4\pi r}\bigg\{[\mathbf{n}\times[\mathbf{p}\times\mathbf{n}]] + \frac{1}{c}[\mathbf{m}\times\mathbf{n}] + \frac{ik}{2}[\mathbf{n}\times[\mathbf{n}\times(\hat{Q}\mathbf{n})]] + \frac{ik}{2c}[\mathbf{n}\times(\hat{M}\mathbf{n})] + \cdots\bigg\}. \quad (6)$$

Here, we introduced the vector of electric dipole (ED) moment $\mathbf{p}$, the vector of magnetic dipole (MD) moment $\mathbf{m}$, the tensor of electric quadrupole (EQ) moment $\hat{Q}$, and the tensor of magnetic quadrupole (MQ) moment $\hat{M}$. Moreover, $c = 1/\sqrt{\mu_0\varepsilon_0\varepsilon_s}$ is the speed of light in the surrounding medium (μ_0 is the vacuum permeability). The dipole and quadrupole moments are determined by [44,46]

$$\mathbf{p} = \int_{V_{\rm p}} j_0(kr)\mathbf{P}d\mathbf{r} + \frac{k^2}{2}\int_{V_{\rm p}}\frac{j_2(kr)}{(kr)^2}[3(\mathbf{r}\cdot\mathbf{P})\mathbf{r} - r^2\mathbf{P}]d\mathbf{r}, \quad (7)$$

$$\mathbf{m} = -i\omega\frac{3}{2}\int_{V_{\rm p}}\frac{j_1(kr)}{kr}[\mathbf{r}\times\mathbf{P}]d\mathbf{r}, \quad (8)$$

$$\hat{Q} = 3\int_{V_{\rm p}}\frac{j_1(kr)}{kr}[3(\mathbf{rP}+\mathbf{Pr}) - 2(\mathbf{r}\cdot\mathbf{P})\hat{1}]d\mathbf{r} + 6k^2\int_{V_{\rm p}}\frac{j_3(kr)}{(kr)^3}[5(\mathbf{r}\cdot\mathbf{P})\mathbf{rr} - r^2(\mathbf{Pr}+\mathbf{rP}) - r^2(\mathbf{r}\cdot\mathbf{P})\hat{1}]d\mathbf{r}, \quad (9)$$

$$\hat{M} = -5i\omega\int_{V_{\rm p}}\frac{j_2(kr)}{(kr)^2}([\mathbf{r}\times\mathbf{P}]\mathbf{r} + \mathbf{r}[\mathbf{r}\times\mathbf{P}])d\mathbf{r}. \quad (10)$$

Note that Eq. (6) with the inclusion of higher order multipoles can be found in [44]. Using (6), the scattered power $W_{\rm sc}$ can be presented as

$$W_{\rm sc} = \frac{1}{2}\sqrt{\frac{\varepsilon_0\varepsilon_s}{\mu_0}}\int_{\Omega}|\mathbf{E}_{\rm sc}(\mathbf{r})|^2 r^2 d\Omega = \frac{k^4 c}{12\pi\varepsilon_0\varepsilon_s}|\mathbf{p}|^2 + \frac{k^4}{12\pi\varepsilon_0\varepsilon_s c}|\mathbf{m}|^2 + \frac{k^6}{160\,\pi\varepsilon_0\varepsilon_s c}||\hat{M}||^2 + \frac{k^6 c}{1440\pi\varepsilon_0\varepsilon_s}||\hat{Q}||^2 + \cdots, \quad (11)$$

where Ω is the total solid angle, $d\Omega = \sin\theta d\theta d\varphi$, and $||\cdot||^2$ is the sum of the squares of the absolute values of all tensor components. The scattering cross-section is $\sigma_{\rm sc} = W_{\rm sc}/W_0$, where W_0 is the intensity of the incident wave.

Note that the above expressions allow one to analyze the contribution of various multipole moments to the scattered field, which will be used in this study.

B. Multipole analysis of periodic 2D arrays

Along with COMSOL Multiphysics for the numerical calculation of the reflection, transmission, and absorption spectra of periodic arrays of hybrid particles, we also use the analytical multipole approach to provide physical insights into the observed spectral features. In a two-dimensional periodic array of identical particles illuminated at normal incidence with a linearly polarized plane wave, all particles are in equivalent conditions. Therefore, all particles exhibit the same multipolar response. In such a setting, numerical simulations can be done for one unit cell while assuming periodic boundary conditions. It suffices to consider the electric field inside the particle to calculate the induced multipole moments. Therefore, the above Eqs. (7)–(10) obtained for single particles can be used to calculate the multipole moments of particles forming an array [47].

With the knowledge of the multipole moments, the reflection and transmission coefficients for the fields can be represented as a superposition of multipole contributions. When the $xy-$plane of the Cartesian coordinate system is aligned with the array plane, and the wavelength of the incident waves is longer than the array periods, i.e., the array is subwavelength, the reflection r_e and transmission t_e coefficients of the electric field can be written in different representations [47] depending on the polarization of the incident plane wave. Assuming a propagation into the $+z$-direction (see Fig. 2), the optical response for an x-polarization of the incident field can be written as

$$r_e = \frac{ik}{E_0 2S_L\varepsilon_0\varepsilon_s}\left(p_x - \frac{1}{c}m_y + \frac{ik}{6}Q_{xz} - \frac{ik}{2c}M_{yz}\right), \quad (12)$$

$$t_e = 1 + \frac{ik}{E_0 2S_L\varepsilon_0\varepsilon_s}\left(p_x + \frac{1}{c}m_y - \frac{ik}{6}Q_{xz} - \frac{ik}{2c}M_{yz}\right). \quad (13)$$

For a y-polarization of the incident field, the optical response can be written as

$$r_e = \frac{ik}{E_0 2S_L\varepsilon_0\varepsilon_s}\left(p_y + \frac{1}{c}m_x + \frac{ik}{6}Q_{yz} + \frac{ik}{2c}M_{xz}\right), \quad (14)$$

$$t_e = 1 + \frac{ik}{E_0 2S_L\varepsilon_0\varepsilon_s}\left(p_y - \frac{1}{c}m_x - \frac{ik}{6}Q_{yz} + \frac{ik}{2c}M_{xz}\right). \quad (15)$$

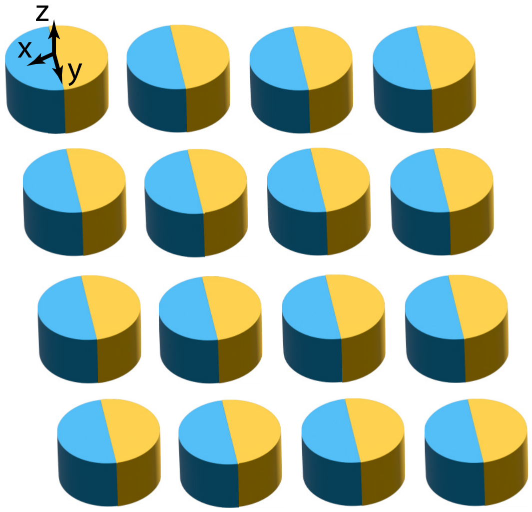

FIG. 2. Schematic illustration of a 2D array composed of hybrid Si-Au cylindrical particles and the orientation of the Cartesian coordinate system.

Here, E_0 is the electric field amplitude of the incident wave in the $xy-$plane ($z = 0$), and S_L is the area of the unit cell. Note that the appearance of a unity in (13) and (15) accommodates the presence of an incident wave. Reflectance (R), transmittance (T), and absorptance (A) are given by

$$R = |r_e|^2, \quad T = |t_e|^2, \quad A = 1 - R - T. \tag{16}$$

Note that the expressions of the transmission and reflection coefficients with the inclusion of higher order multipoles can be found in [48].

III. OPTICAL PROPERTIES OF THE SINGLE PARTICLES

A. Symmetrical analysis

The symmetry analysis of the multipole composition of the eigenmodes of scatterers is a powerful tool for describing the features of their interaction with external radiation and the distribution of scattered electromagnetic fields [49,50]. Therefore, before studying the optical resonances of the particle, we will analyze its symmetry to understand what type of multipolar bianisotropy can be realized in such hybrid particles. To do this we apply the method presented in Refs. [50,51]. In these prior publications, it was argued that each resonator (particle) corresponds to a point symmetry group, and its eigenmodes transform according to the irreducible representations of this group. Moreover, all modes can be decomposed into a set of vector spherical harmonics (VSHs), which transform according to the irreducible representation of this mode. For the definition of VSHs, see Appendix A. Importantly, *a mode sustained by the particle can only be excited if it contains at least one VSH also contained in the incident light*. Since certain VSHs correspond to radiation patterns of certain multipole moments, they can also be called multipoles. If the excited mode of a particle contains multipoles of a parity different than the excitation, the system offers a bianisotropic response [51]. The latter arises in particles without spatial inversion symmetry.

The cylindrical hybrid particle presented in Fig. 1 has C_{2v} symmetry. The sets of its eigenmodes, distributed over the irreducible representations, and their corresponding VSHs contents are presented in Appendix B. Note that such a point symmetry group also corresponds to an isosceles prism made of homogeneous material [51]. The multipolar content of a plane electromagnetic wave, depending on the direction of propagation and polarization, can be found in Appendix B. Comparing the contents of the VSHs in the two tables (Appendix B, Fig. 10), we can obtain complete information about which modes and, consequently, which multipole moments will be excited by a plane wave depending on its direction of incidence and polarization.

As an example, let us focus on a dipole-dipole coupling between the incident plane wave and the modes of the hybrid particle, which can lead to a dipolar bianisotropy.

First, we indicate a relation between the dipole moments and VSHs:

$$\begin{array}{ll} p_x \rightarrow \mathbf{N}_{e11} & m_x \rightarrow \mathbf{M}_{e11} \\ p_y \rightarrow \mathbf{N}_{o11} & m_y \rightarrow \mathbf{M}_{o11} \\ p_z \rightarrow \mathbf{N}_{e01} & m_z \rightarrow \mathbf{M}_{e01}. \end{array} \tag{17}$$

From the tables in Fig. 10, one can see that the incident (k_z, E_x, H_y)-wave contains two dipolar VSHs ($\mathbf{N}_{e11}$ and $\mathbf{M}_{o11}$) and, consequently, excites the A_1 (with $\mathbf{N}_{e11}$) mode and B_1 (with $\mathbf{M}_{o11}$) mode, respectively. The B_1-mode, being excited by $\mathbf{M}_{o11}$ of the incident wave, contains $\mathbf{N}_{e01}$ (p_z), which is not present in the incident wave. Consequently, a z-polarized dipole moment p_z is induced in the particle. Such a response can be explained by a dipolar bianisotropic response as [51]

$$p_z = c^{-1}\alpha_{zy}^{\mathrm{em}} H_y(\mathbf{r}_0). \tag{18}$$

Here, $\alpha_{zy}^{\mathrm{em}}$ is a component of the bianisotropic polarizability, and $H_y(\mathbf{r}_0)$ is the incident magnetic field at the position $\mathbf{r}_0$ of the dipole moment.

In this paper, we assume that *all multipole moments of the hybrid nanocylinder are located at its geometric center*. Thus, $\mathbf{r}_0$ points to the particle center, and if the origin of the coordinate system is located in this center, then $\mathbf{r}_0 = 0$.

Similarly (see the tables in Fig. 10), the incident (k_z, E_y, H_x)-wave excites A_2 and B_2 modes. The B_2-modes, being excited by $\mathbf{N}_{o11}$ of the incident wave, contains $\mathbf{M}_{e01}$ (m_z), which is present in the multipole decomposition of the incident wave. Therefore, we can conclude that the appearance of m_z in the particle's response will be again a result of the dipole bianisotropic property [51]:

$$m_z = c\alpha_{zy}^{\mathrm{me}} E_y(\mathbf{r}_0). \tag{19}$$

Here, $\alpha_{zy}^{\mathrm{me}}$ is a component of the bianisotropic polarizability, and $E_y(\mathbf{r}_0)$ is the incident electric field at the position $\mathbf{r}_0$ of the dipole moment.

From the Onsager-Casimir conditions [52], we have to conclude that

$$\alpha_{zy}^{\mathrm{em}} = -\alpha_{yz}^{\mathrm{me}}, \quad \alpha_{zy}^{\mathrm{me}} = -\alpha_{yz}^{\mathrm{em}}. \tag{20}$$

It is important that the dipole components p_x ($\mathbf{N}_{e11}$) and m_x ($\mathbf{M}_{e11}$) are contained in the A_1 and A_2 modes, respectively, and are the only dipole components of these

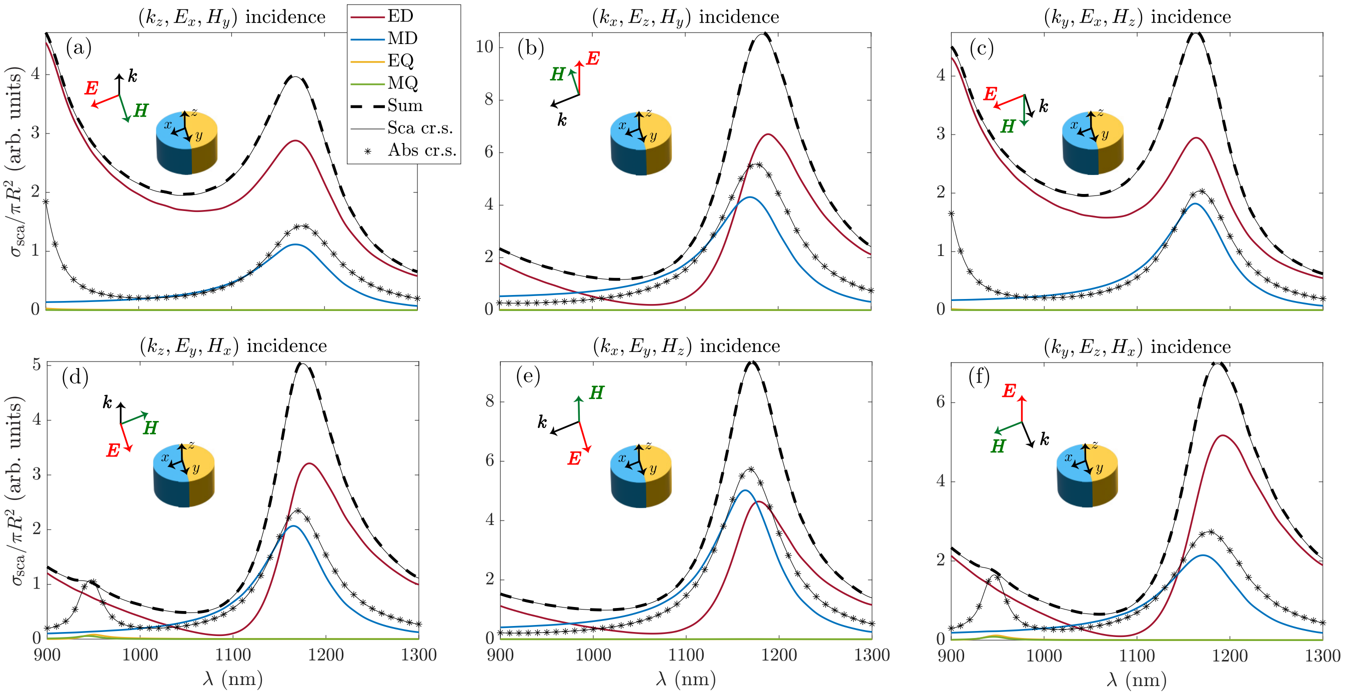

FIG. 3. Scattering ($\sigma_{\rm sca}$) and absorption ($\sigma_{\rm abs}$) cross-sections and corresponding multipole contributions to the scattering cross-sections (SCSs) calculated by COMSOL for different illumination conditions (see in the title of every panel): k_x (k_y and k_z) is the wave vector component corresponding to the incident direction and E_x (E_y and E_z) corresponds to the polarization direction of the incident plane waves. "Sum" is the SCS calculated as the sum of the multipole contributions (11).

modes. Therefore, they cannot be excited due to the dipole-dipole bianisotropy. Indeed, mode A_1 does not include a magnetic dipole, so it cannot be excited by a magnetic dipole of incident waves. In contrast, mode A_2 does not include an electric dipole, so it cannot be excited by an electric dipole of incident waves. So we can conclude that

$$\alpha^{\rm em}_{xy} = \alpha^{\rm me}_{xz} = \alpha^{\rm me}_{xy} = \alpha^{\rm em}_{xz} = 0. \tag{21}$$

A complete symmetry analysis of the dipole bianisotropy leads us to an important result regarding the dipole polarizability tensor $\hat{\alpha}$:

$$\hat{\alpha} = \begin{pmatrix} \alpha^{\rm ee}_{xx} & 0 & 0 & 0 & 0 & 0 \\ 0 & \alpha^{\rm ee}_{yy} & 0 & 0 & 0 & c^{-1}\alpha^{\rm em}_{yz} \\ 0 & 0 & \alpha^{\rm ee}_{zz} & 0 & c^{-1}\alpha^{\rm em}_{zy} & 0 \\ 0 & 0 & 0 & \alpha^{\rm mm}_{xx} & 0 & 0 \\ 0 & 0 & c\alpha^{\rm me}_{yz} & 0 & \alpha^{\rm mm}_{yy} & 0 \\ 0 & c\alpha^{\rm me}_{zy} & 0 & 0 & 0 & \alpha^{\rm mm}_{zz} \end{pmatrix}, \tag{22}$$

where the following expression explains the action of the tensor $\hat{\alpha}$:

$$\begin{pmatrix} \mathbf{p} \\ \mathbf{m} \end{pmatrix} = \hat{\alpha} \begin{pmatrix} \varepsilon_0 \varepsilon_s \mathbf{E} \\ \mathbf{H} \end{pmatrix} = \begin{pmatrix} \hat{\alpha}^{\rm ee} & c^{-1}\hat{\alpha}^{\rm em} \\ c\hat{\alpha}^{\rm me} & \hat{\alpha}^{\rm mm} \end{pmatrix} \begin{pmatrix} \varepsilon_0 \varepsilon_s \mathbf{E} \\ \mathbf{H} \end{pmatrix}. \tag{23}$$

Here, $\mathbf{E}$ and $\mathbf{H}$ are the electric and magnetic fields of the incident wave at the point of the dipole moment localization. Note that (22) is a general formula for the dipole polarizability tensor for particles with the symmetry C_{2v}. In the next subsection, we will test our findings concerning polarizability tensor using analytical and numerical approaches.

Thus, from the symmetry consideration, it follows that the bianisotropic p_z (m_z) component of the electric (magnetic) dipole moment will be excited by a plane wave incident along the z-axis with a magnetic (electric) field directed along the interface between the gold and silicon parts of the particle. In the first case, we can talk about electrical bianisotropic response, and in the second case, about magnetic bianisotropic response.

B. Dipole resonances and polarizabilities

Here, we consider the multipole response of a hybrid particle with a radius of $R = 100$ nm and a height of $H = 200$ nm. The absorption and scattering cross-sections and the corresponding multipole contributions calculated for different illumination conditions are presented in Fig. 3. In almost the entire considered wavelength range, i.e., $900 - 1300$ nm, the quadrupolar contribution is negligible compared to the dipole contribution for all incident wave configurations. Also, all higher-order multipoles are negligible. Only in Fig. 3(d) and in Fig. 3(f) at $\lambda \approx 960$ nm, can one see weak resonant contributions of the MQ and EQ response to the scattering. Although the values of these contributions are small in the scattering, their excitation gives rise to non-negligible absorption resonances [Figs. 3(d) and 3(f)]. Later, we will observe the same effect for arrays made from these particles. Note that the infrared frequency range was chosen since silicon is lossless, and the metal part determines all absorption in the system.

The symmetry analysis above showed that incident plane wave (k_z, E_x, H_y) excites the A_1 and B_1 modes with the

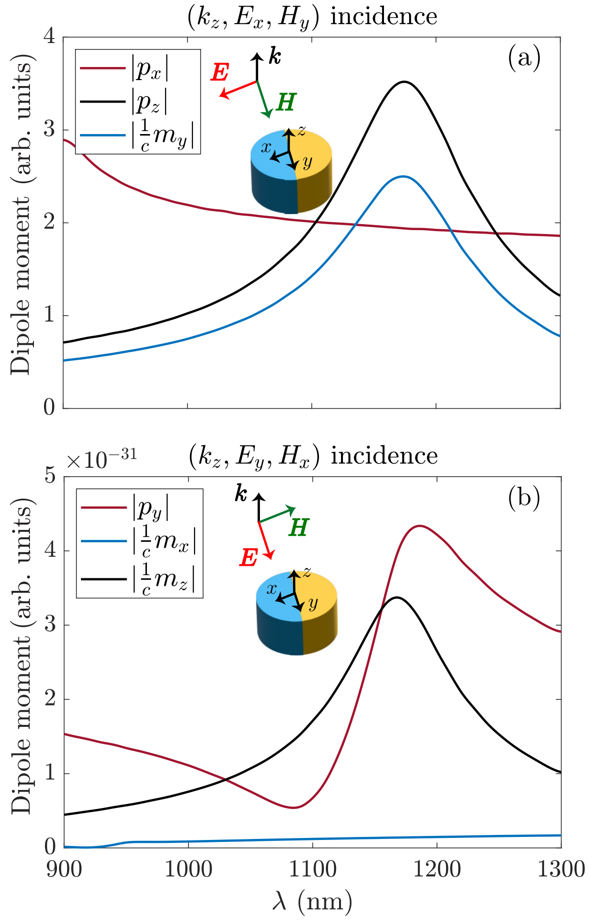

FIG. 4. ED and MD components contributing to the electromagnetic response of the hybrid cylinder. The insets show the illumination conditions of an incident plane wave. The polarization of the incident electric field is along the x-axis in (a) and along the y-axis in (b).

dipole components p_x, m_y, and p_z, while other dipole components' contribution to the scattering should be absent. In Fig. 4(a), one can see that, indeed, only these components of the dipoles are excited. Dipole moments were calculated using Eqs. (7), (8).

Similarly, the incident wave (k_z, E_y, H_x) excites the A_2 and B_2 modes. Therefore, p_y, m_x, and m_z should be excited. Figure 4(b) confirms that. The observation means that the abovementioned general symmetry analysis works for inhomogeneous particles.

Here, we make an important remark regarding the spectral position of the resonant dipole responses shown in Fig. 4. It can be seen that the resonance of the bianisotropic components of the electric p_z and magnetic m_z dipole moments occur at the same wavelength. It follows that the modes of the hybrid particle that include these dipole components are degenerate, and the polarization of the incident wave determines their excitation. Note, as shown below, such particles can be used to construct metasurfaces with the effect of polarization switching between magnetic- and electric-type quasi-BICs [37].

Now let us show how one can determine the polarizability from (22) and (23). For that, we will use the results of the numerical calculation of the dipole moments $\mathbf{p}$ and $\mathbf{m}$, and the approach given in Refs. [53,54].

For the incident condition (k_z, E_x, H_y) from (23) with (22) one obtains $p_z = c^{-1}\alpha_{zy}^{\mathrm{em}} H_y(\mathbf{r}_0)$, this leads to

$$\alpha_{zy}^{\mathrm{em}} = p_z c / H_y(\mathbf{r}_0). \tag{24}$$

For the incident conditions (k_z, E_y, H_x) one also obtains $m_z = c\varepsilon_0\varepsilon_s\alpha_{zy}^{\mathrm{me}} E_y(\mathbf{r}_0)$, and

$$\alpha_{zy}^{\mathrm{me}} = m_z / c\varepsilon_0\varepsilon_s E_y(\mathbf{r}_0). \tag{25}$$

From the Onsager-Casimir conditions (20) we also determine $\alpha_{yz}^{\mathrm{me}}$ and $\alpha_{yz}^{\mathrm{em}}$.

For the incident conditions $(+k_x, E_z, H_y)$ and $(-k_x, E_z, -H_y)$ one can write, respectively,

$$p_z^{(+)} = \varepsilon_0\varepsilon_s\alpha_{zz}^{\mathrm{ee}} E_z(\mathbf{r}_0) + c^{-1}\alpha_{zy}^{\mathrm{em}} H_y(\mathbf{r}_0), \tag{26}$$

$$p_z^{(-)} = \varepsilon_0\varepsilon_s\alpha_{zz}^{\mathrm{ee}} E_z(\mathbf{r}_0) - c^{-1}\alpha_{zy}^{\mathrm{em}} H_y(\mathbf{r}_0), \tag{27}$$

where we have introduced the notations $p_z^{(+)}$ and $p_z^{(-)}$ for the ED z-components calculated for the incident wave propagating along the positive $+k_x$ and negative $-k_x$ directions of the x-axis, respectively. Note that the amplitude of the electric field E_z of the incident wave does not change sign when the direction of incidence changes.

For the incident conditions (k_x, E_y, H_z) and $(-k_x, E_y, -H_z)$ one can write, respectively,

$$m_z^{(+)} = \alpha_{zz}^{\mathrm{mm}} H_z(\mathbf{r}_0) + c\varepsilon_0\varepsilon_s\alpha_{zy}^{\mathrm{me}} E_y(\mathbf{r}_0)\,, \tag{28}$$

$$m_z^{(-)} = -\alpha_{zz}^{\mathrm{mm}} H_z(\mathbf{r}_0) + c\varepsilon_0\varepsilon_s\alpha_{zy}^{\mathrm{me}} E_y(\mathbf{r}_0)\,, \tag{29}$$

where we used the same designation rules as above.

Using pairs of Eqs. (26)–(27) and (28)–(29) it is easy to get

$$\alpha_{zz}^{\mathrm{ee}} = \frac{p_z^{(+)} + p_z^{(-)}}{2\varepsilon_0\varepsilon_s E_z(\mathbf{r}_0)}, \tag{30}$$

$$\alpha_{zz}^{\mathrm{mm}} = \frac{m_z^{(+)} - m_z^{(-)}}{2H_z(\mathbf{r}_0)}. \tag{31}$$

By applying a similar approach as above for other incident wave directions and polarizations, the other remaining polarizabilities $\alpha_{yy}^{\mathrm{mm}}$, $\alpha_{yy}^{\mathrm{ee}}$, $\alpha_{xx}^{\mathrm{ee}}$, and $\alpha_{xx}^{\mathrm{mm}}$ are also calculated. Note that the polarizabilities calculated in this way include both the static part and the contribution from the local density of states [55] as well as bianisotropic features of the magnetoelectric dipole scatterer [56].

IV. METASURFACES

In this section, we consider the optical properties of the metasurfaces composed of the resonant hybrid cylinders (Fig. 2) illuminated at normal incidence with an x- or y-polarized plane wave. The transmission T and reflection R coefficient are calculated using COMSOL Multiphysics. The contributing multipole moments are identified with Eqs. (12)–(15).

A. Tuning the metasurface period

To identify the period of the metasurface that supports a quasi-BIC, we use the method from Ref. [37]. In short, the

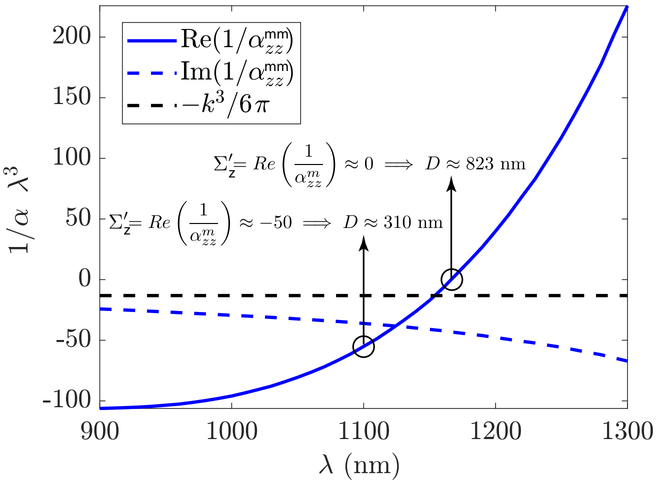

FIG. 5. The real (blue solid line) and imaginary (blue dashed line) parts of the inverse of the magnetic dipole polarizability tensor component α_{zz}^{mm}. The black dashed line corresponds to the imaginary part of the inverse dipole polarizability $k_0^3/6\pi$ when the electromagnetic response of the system is local, i.e., multiples of the second order and higher are negligible. The circles indicate the wavelengths at which a quasi-BIC is excited in the array.

method is based on comparing the real part of the inverse dipole polarizability $\alpha_{zz}^{\mathrm{ee}}$ or $\alpha_{zz}^{\mathrm{mm}}$ for the normal component of the electric or magnetic dipole moment, respectively, with the lattice sum $\sum_z$, expressing the interaction of these components in the metasurface array with a square unit cell. A magnetic quasi-BIC in dipole approximation is excited when

$$\mathrm{Re}\left(\frac{1}{\alpha_{zz}^{\mathrm{mm}}}\right) = \sum\nolimits_z' \quad \text{for the magnetic BIC,} \tag{32}$$

where $\sum_z'$ is the real part of the full lattice sum $\sum_z$. Replacing $\alpha_{zz}^{\mathrm{mm}}$ in (32) with $\alpha_{zz}^{\mathrm{ee}}$, we obtain the condition for the electric BIC. Since, unlike the polarizabilities of a single particle, the sum $\sum_z'$ depends on the metasurface period, it can be determined from Eq. (32) for a fixed wavelength. From a practical point of view, this equation is easier to solve graphically by determining the points where the values of $\mathrm{Re}(1/\alpha_{zz}^{\mathrm{mm}})$ and $\sum_z'$ coincide. Note, that Eq. (32) resembles the surface lattice resonance condition [57], but with one fundamental difference. This equation includes the lattice sum corresponding to the interaction between equivalent dipole moments oriented perpendicular to the plane of the metasurface. Since these dipoles do not radiate waves away from the metasurface, this equation corresponds to the condition of the existence of a nonradiative dipole eigenmode of the metasurface or a symmetrically protected bound state in the continuum in the dipole approximation [58].

The analytical expression and general plot of the normalized sum $[\lambda^3\sum_z']$ as a function of the ratio of the period to the wavelength D/λ is presented in [37]. By choosing the value of $[\lambda^3\mathrm{Re}(1/\alpha_{zz}^{\mathrm{mm}})]$, marked by circles in Fig. 5, and taking the same values for $[\lambda^3\sum_z']$ (Fig. 1 in Ref. [37]), we find the corresponding values of the period D for the metasurfaces. These metasurfaces will have a resonant magnetic quasi-BIC response at the wavelengths corresponding to the chosen values of $\mathrm{Re}(1/\alpha_{zz}^{\mathrm{mm}})$. As shown in the inset of Fig. 5, to obtain a magnetic quasi-BIC resonance at $\lambda \approx 1160$ nm where $[\lambda^3\mathrm{Re}(1/\alpha_{zz}^{\mathrm{mm}})] \approx 0$, the period D must be equal to 823 nm. There, also shown, to obtain a magnetic quasi-BIC resonance at $\lambda \approx 1100$ nm, where $[\lambda^3\mathrm{Re}(1/\alpha_{zz}^{\mathrm{mm}})] = -50$, the period D must be equal 310 nm.

Note that the equality

$$\mathrm{Re}\left(\frac{1}{\alpha_{zz}^{\mathrm{mm}}}\right) = 0 \tag{33}$$

corresponds to the resonance value of the magnetic dipole polarizability $\alpha_{zz}^{\mathrm{mm}}$ of a single particle at the corresponding resonance wavelength λ^{Res}. Under these conditions, as was shown in [37], the period D of the metasurface with the symmetry-protected BIC at this wavelength is determined by the "rule of 0.71", that is, $D \approx 0.71\lambda^{\mathrm{Res}}$. This rule is followed from the fact that the dipole sum $\sum_z'$ for a lattice with a square unit cell is always equal to 0 when $D/\lambda \approx 0.71$, where λ is the wavelength in the surrounding media [37]. By identifying the wavelength at which the real part of the dipole polarizability $\alpha_{zz}^{\mathrm{mm}}$ ($\alpha_{zz}^{\mathrm{ee}}$) of a single scatterer also equals 0, we can determine the metasurface period for which resonant magnetic (electric) quasi-BIC excitation occurs at this specific wavelength [see Eq. (32)].

The "rule of 0.71" is fulfilled for the implementation of the magnetic BIC at a wavelength $\lambda = 1160$ nm in a metasurface with a period of $D = 823$ nm $(823/1160 \approx 0.71)$. In this case, $\lambda = 1160$ nm is the resonant wavelength λ^{Res} for the excitation of m_z, as follows from the MD contributions to the scattering cross section shown in Figs. 3(c) and 3(e).

Next, we will consider metasurfaces with periods of 823 nm and 310 nm. It will be shown that for a period of 823 nm and a wavelength of 1160 nm, both magnetic and electric quasi-BICs are excited depending on the polarization of the incident wave. This behavior is due to the fact that the resonances of $\alpha_{zz}^{\mathrm{mm}}$ and $\alpha_{zz}^{\mathrm{ee}}$ overlap in this part of the spectrum (Fig. 3).

B. Nonabsorbing case

To demonstrate the applicability of the above-described method for determining the metasurface period, let us consider a hypothetical case where the absorption of light in the hybrid particles is significantly suppressed. To do this, we will artificially reduce the imaginary parts of the permittivities of gold and silicon during the modeling by multiplying them by 0.01. For this *lossless* case, the results of the COMSOL calculation of the transmission, reflection, and absorbance spectra for metasurfaces with periods of 823 nm and 310 nm are presented in Fig. 6. It is clearly seen that for the period of 823 nm [Fig. 6(a)] and the period of 310 nm [Fig. 6(b)], the transmission (reflection) is resonantly suppressed (increased) at wavelengths of ~1160 nm and ~1100 nm, respectively. Such resonant behavior, in turn, fully corresponds to the wavelengths to which the quasi-BICs are tuned. Therefore, the suppression of transmission and the resonant enhancement of reflection to almost unity in these cases is associated with the excitation of quasi-BICs of the magnetic type. The polarization of the incident wave determines the type of quasi-BICs (see also discussion below). Note that the narrow resonances

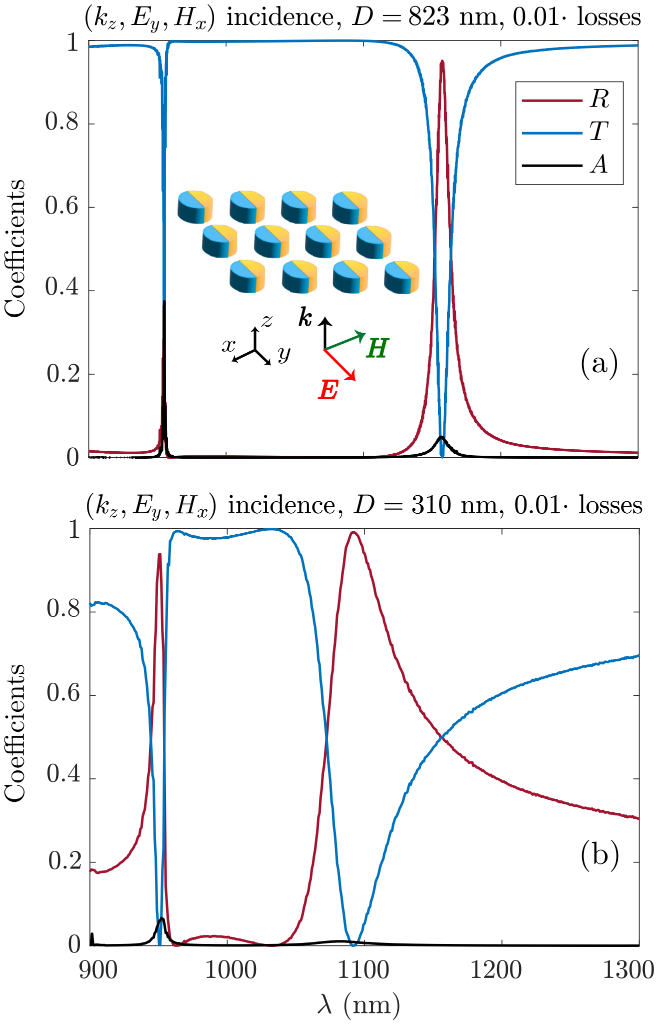

(k_z, E_y, H_x) incidence, $D = 823$ nm, $0.01\cdot$ losses

(k_z, E_y, H_x) incidence, $D = 310$ nm, $0.01\cdot$ losses

FIG. 6. Reflectance (R), transmittance (T), and absorptance (A) for the configuration of the incident plane wave (k_z, E_y, H_x) and the period of the structure (a) $D = 823$ nm; (b) $D = 310$ nm. The relative permittivity $\varepsilon = \varepsilon' + 0.01 \cdot \varepsilon''$ for both materials, where ε', ε'' are the real and imaginary parts of the relative permittivity.

in Fig. 6 at shorter wavelengths are due to the quadrupole resonance of the single particle (see Fig. 3). These narrow resonances are not related to the quasi-BICs under consideration.

C. Transmission, reflection, absorption

Now, let us return to metasurfaces composed of hybrid particles while considering their permittivities as they are, i.e., without multiplying the imaginary parts with a factor smaller than one. All spectra discussed below are calculated using COMSOL and the multipole approximation described above in Eqs. (12)–(15). Since there is excellent agreement between the results obtained using both approaches, we will use the multipole analysis in the following to explain the observed spectral features.

The spectra of R, T, and A of the metasurface with the period $D = 823$ nm and for two illumination conditions are shown in Fig. 7. It is seen that, as follows from the period setting, the resonant features associated with the quasi-BIC are excited at a wavelength of $\lambda = 1160$ nm independently on the polarization of the incident wave [compare Fig. 7(a) and Fig. 7(c)]. In this case, in contrast to the nonabsorbing case (Fig. 6), a resonant absorption band appears. The spectral position of the absorption resonances is also independent of the polarization of the incident wave. Such behavior is associated only with the resonant dipole response of hybrid particles in the metasurface. Figures 7(b) and 7(d) show the multipole contributions to the reflection r_e and transmission t_e coefficients, as well as the resonant values of the bianisotropic dipole components m_z and p_z, respectively.

One can see that the dipole moments provide the main contributions in both illumination conditions. Since out-of-plane dipole components m_z or p_z cannot directly generate radiation from the metasurface plane, they are not included in the expressions for the reflection and transmission coefficients (12)–(15). Their resonant excitation leads to the realization of magnetic (in Fig. 7(a) with m_z) and electric (in Fig. 7(c) with p_z) quasi-BICs and the formation of absorption bands around $\lambda \approx 1160$ nm. *Thus, the excitation of the quasi-BIC mode in hybrid metasurfaces appears as the absorption resonance.* If the electric (magnetic) field of the incident wave is directed along the gold-silicon interface, a magnetic (electric) quasi-BIC is excited in the system.

The realization of the absorption resonances (associated with different-type quasi-BICs) in the same spectral region in Fig. 7(a) and Fig. 7(c) leads to the possibility of the polarization switching between them. This became possible due to the coincidence of the resonant wavelength λ^{Res} for p_z and m_z of a single particle (Fig. 4), as well as due to the application of the procedure for tuning the metasurface period. Let us emphasize once again that we have achieved the effect of polarization switching between magnetic and electrical trapped modes (quasi-BIC modes), which in turn led to the appearance of a polarization-independent resonant absorption band.

Another interesting feature of the spectra presented in Fig. 7 is the Fano profile of the reflection resonances in the quasi-BIC region around $\lambda = 1160$ nm. Note that the spectral hierarchy of the positions of the maximum and minimum of reflection is different for the two illumination conditions [compare R in Figs. 7(a) and 7(c)]. The basis of this difference is that these Fano resonances are associated with the manifestation of different effects: the anapole effect in Fig. 7(a) and the Kerker effect in Fig. 7(c). Indeed, in the first case, from the multipole contributions shown in Fig. 7(b), we see that the reflection coefficient can be written as

$$r_e \approx \frac{ik}{E_0 2 S_L \varepsilon_0 \varepsilon_s} p_y, \tag{34}$$

because only p_y provides the main resonant contribution. However, as shown in Fig. 7(b), p_y is significantly suppressed around $\lambda = 1090$ nm, due to an anapole effect [8,38], leading to a Fano profile of the $|p_y|$ resonance in Fig. 7(b) and the corresponding Fano profile of the reflection in Fig. 7(a). In contrast, the reflection coefficient for the case in Fig. 7(c) has two dipole contributions

$$r_e \approx \frac{ik}{E_0 2 S_L \varepsilon_0 \varepsilon_s} \left(p_x - \frac{1}{c} m_y \right). \tag{35}$$

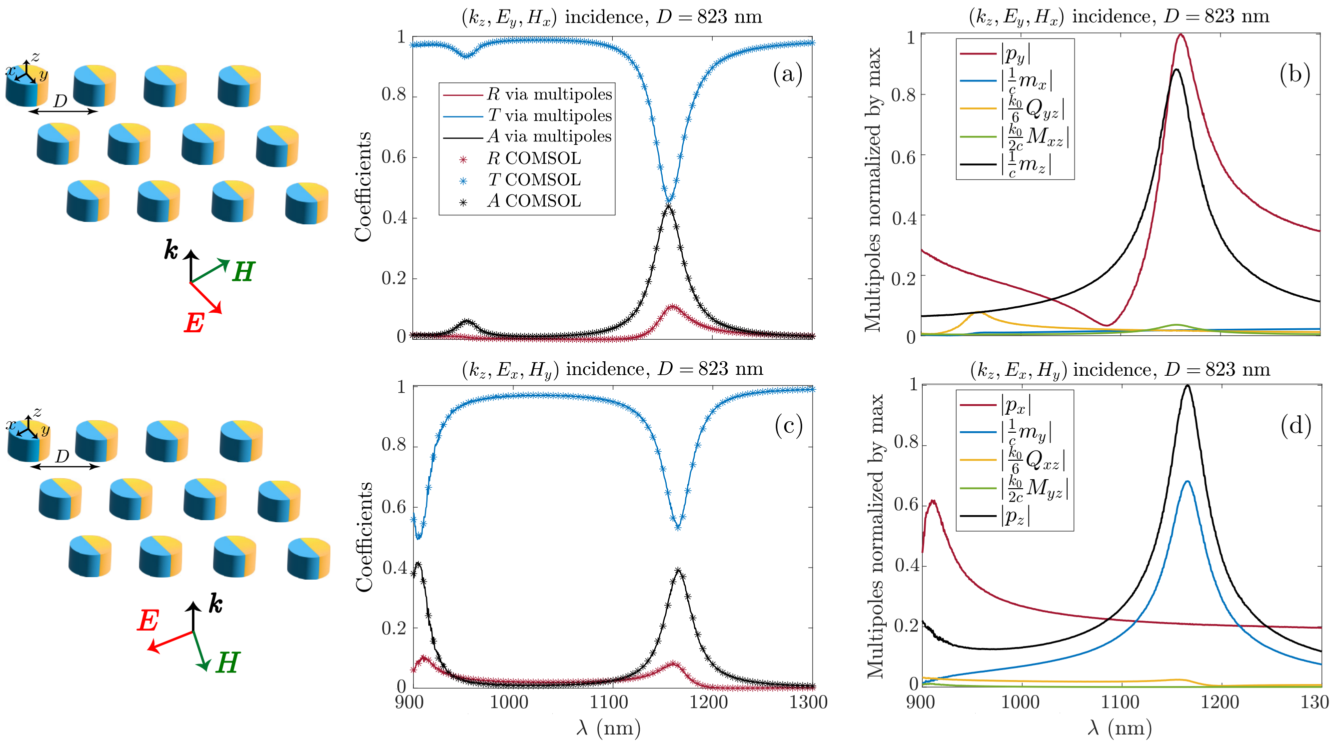

FIG. 7. Reflectance (R), transmittance (T), and absorptance (A) calculated using COMSOL and via the multipolar decomposition for the period of the structure $D = 823$ nm and the configuration of the incident plane wave (a) (k_z, E_x, H_y), (c) (k_z, E_y, H_x). The spectrum of the components of multipoles contributions to R, T, and A normalized to the maximal value of all (b) (k_z, E_x, H_y), (d) (k_z, E_y, H_x). The insets on the left show the plane wave incidence direction and polarization, as well as the metasurface consisting of silicon-gold cylinders [top for (a) and (b), bottom for (c) and (d)].

Therefore, the suppression of the reflection, leading to the Fano resonance profile, is realized due to the Kerker condition $p_x = m_y/c$ [8] that is satisfied around $\lambda = 1200$ nm. It is crucial for experimental purposes to determine the spectral positions of reflectance suppression points, as measuring reflectance is typically easier than measuring absorption. By identifying the boundaries between resonant reflection and suppression, we can infer the location of the absorption resonance. In conclusion of the discussion of the results presented in Fig. 7, we note that the resonances arising at shorter wavelengths closer to $\lambda = 900$ nm are not associated with the excitation of any quasi-BIC modes and are a consequence of the direct excitation of certain multipole moments [electric quadrupole in Fig. 7(a) and electric dipole in Fig. 7(c)].

Now let us consider the metasurface with a smaller period $D = 310$ nm for two different illumination conditions, i.e., once polarized in y-direction (k_z, E_y, H_x) and once polarized in x-direction (k_z, E_x, H_y), respectively, as shown in Fig. 8. In general, the results presented in Fig. 8 for $D = 310$ nm are qualitatively similar to those in Fig. 7 for $D = 823$ nm, the differences concern the spectral red shift of resonances and their smaller quality factors. From Figs. 8(a) and 8(c), one can see that the resonant absorption bands are realized around $\lambda = 1100$ nm and correspond to the broad resonance of the out-of-plane magnetic m_z and electric p_z dipole components, respectively, [see Figs. 8(b) and 8(d)]. As in the previous example for $D = 823$ nm, these absorption bands are related to the excitation of the magnetic and electric quasi-BICs, respectively. However, the spectral position of the absorption band maxima does not coincide, indicating that for $D = 310$ nm, the electric and magnetic quasi-BIC modes are excited at different wavelengths. This difference is caused by the difference between the values of $\alpha_{zz}^{\mathrm{mm}}$ and $\alpha_{zz}^{\mathrm{ee}}$ around $\lambda = 1100$ nm. Note that, as in the case shown in Fig. 7, here the quasi-BICs are excited due to the corresponding bianisotropic coupling between the out-of-plane and in-plane components of the electric and magnetic dipole moments. Therefore, the resonant behavior of p_y in Fig. 8(b) and m_y in Fig. 8(d) is consistent with the resonances of m_z and p_z, respectively, associated with the excitation of the corresponding magnetic and electric quasi-BIC modes.

The reasons for the occurrence of wide Fano resonances in the reflection spectra of the metasurface with $D = 310$ nm (Fig. 8) are the same as in Fig. 7 for the metasurface with $D = 823$ nm. Moreover, the absorption band in the region of $\lambda = 950$ nm in Fig. 8(a) is also a consequence of the resonant excitation of the electric quadrupole moment.

D. Energy accumulation under quasi-BICs

An additional nontrivial question concerns the distribution of fields in a metasurface composed of hybrid particles under quasi-BIC conditions. Under these resonance conditions, electromagnetic energy is concentrated in the plane of the metasurface, which can be used to activate various nanoscale processes. The distribution of the electric field normalized on the background field in a single cell of the metasurface with $D = 823$ nm is presented in Fig. 9. In Fig. 9(a), the field is

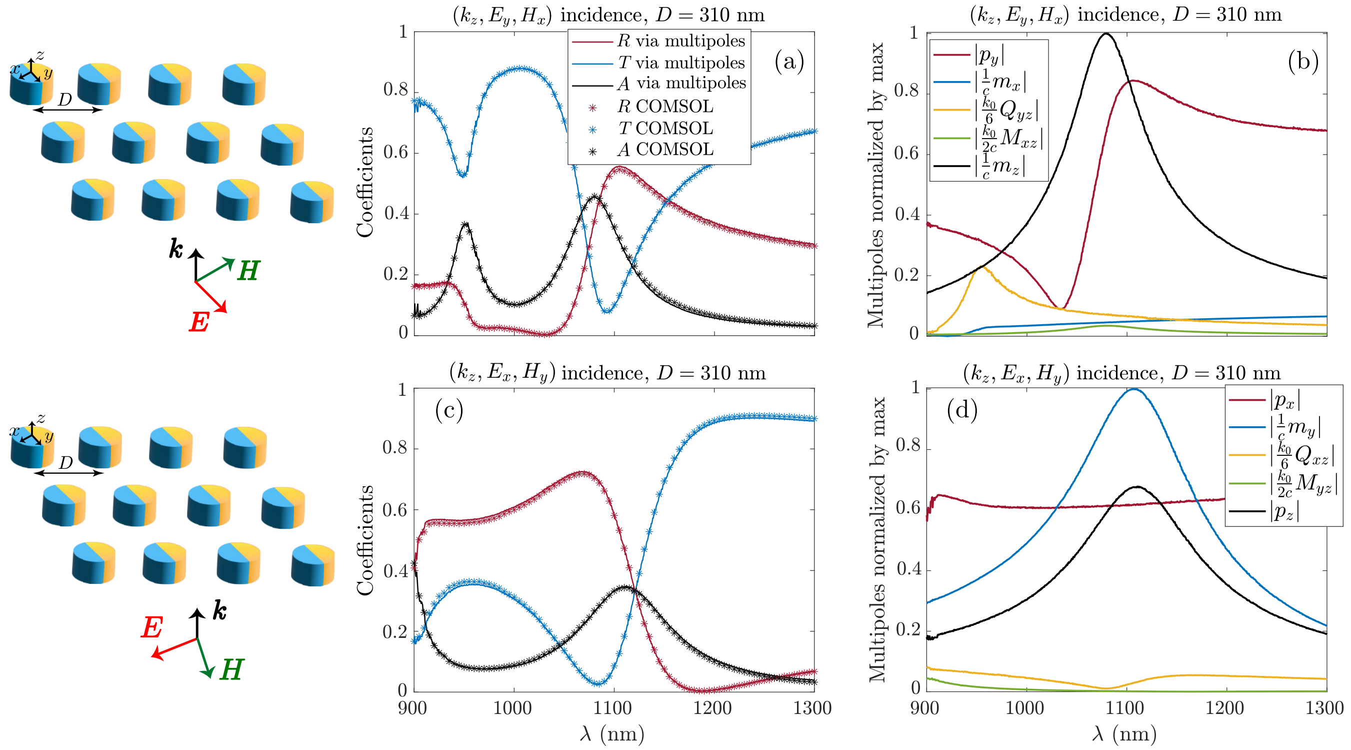

FIG. 8. Same as Fig. 7, but for the structure with the period $D = 310$ nm.

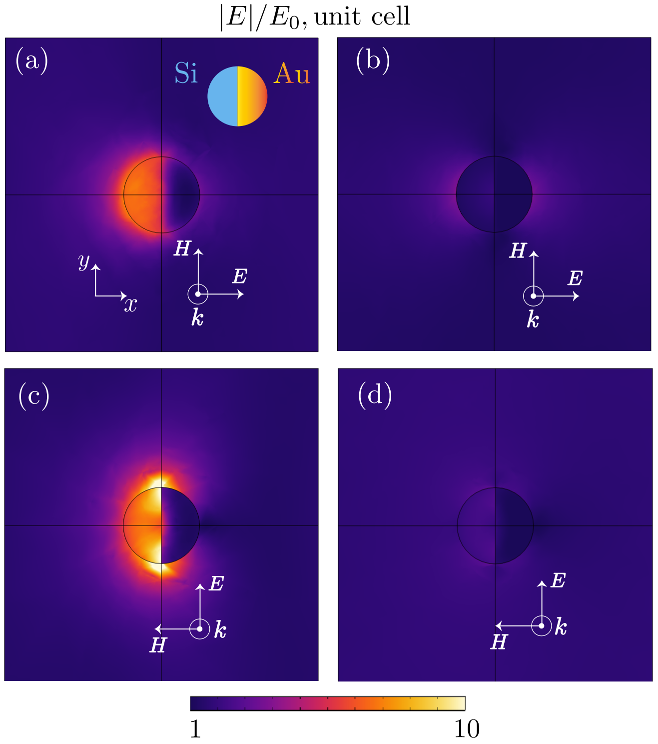

FIG. 9. Normalized electric field amplitude distribution in the middle section of a single unit cell of the hybrid metasurface (period 823 nm) for (a) resonance wavelength 1160 nm and (b) nonresonance wavelength 1050 nm with (k_z, E_x, H_y) incidence; (c) resonant and (d) nonresonant wavelengths with (k_z, E_y, H_x) incidence. Right panel: top view of the silicon and gold cylinder nanoparticle.

plotted at the wavelength of 1160 nm for the (k_z, E_x, H_y) incidence, corresponding to **electric** quasi-BIC. Notably, almost the entire field is concentrated in the dielectric part of the hybrid cylinder. In the metal, the electric field is suppressed.

Moreover, due to the excitation of the quasi-BIC at this wavelength, the field is ≈8 times greater than the incident field. Figure 9(b) presents the electric field at the nonresonance wavelength. In the nonresonance condition, the electric field inside the particle is much weaker than in the resonance wavelength. According to Fig. 7(c), at 1050 nm, the field passes through the metasurface, preserving its amplitude. The same situation is observed for the (k_z, E_y, H_x) excitation. At the resonance wavelength 1160 nm, corresponding to the **magnetic** quasi-BIC resonance, we see the enhancement of the electric field in the dielectric part of the nanoparticle [Fig. 9(c)]. At the same time, no such effect is observed for the nonresonance wavelength in Fig. 9(d). It is compelling to note the difference between the electric field distribution inside the nanocylinder for magnetic and electric quasi-BIC. The field distribution is largely homogeneous in the electric quasi-BIC shown in Fig. 9(a). In contrast, the magnetic quasi-BIC shown in Fig. 9(c) exhibits a more concentrated electric field near the particle boundaries. Additionally, part of the field extends outside the structure, generating strong near-fields.

V. CONCLUSION

Optical properties of individual hybrid (metal-dielectric) cylindrical particles and metasurfaces composed of them were investigated for the manifestation of a resonance response. It was found that the representation of a cylindrical particle in the form of two parts filled with different materials, in particular gold and silicon, leads to the appearance of bianisotropic optical properties in this particle. Combining the analysis of the symmetry properties of the hybrid particle with the multipole composition of its eigenmodes allowed us to obtain information about the dipole polarizability tensor and its bianisotropic components in advance. After numerical calculation of the components of the dipole polarizability tensor, a procedure was applied to determine the period of the metasurface (composed of bianisotropic particles) that supports a resonant response in the view of quasitrapped modes (quasi-BICs) at the required wavelength. It has been shown that the polarization of the incident wave determines the type (electric or magnetic) of the excited quasi-BIC. As a result of modeling the optical properties of metasurfaces under normal illumination, resonance features in the transmission spectra due to quasi-BIC excitation were demonstrated. It was found that, unlike purely dielectric metasurfaces, quasi-BIC excitation in hybrid metasurfaces leads to the resonant absorption of light. Under resonant absorption conditions, strong electromagnetic fields are concentrated in the dielectric part of the hybrid metasurface particles, contributing to transmission and reflection. Dipole analysis of reflection showed that, depending on the polarization of the incident wave, its suppression can be associated with the anapole effect and the Kerker effect. Thus, the obtained results demonstrated the applicability of the quasi-BIC tuning method for systems with hybrid particles and also established a direct relationship between absorption resonances and excitation of trapped modes in the form of quasi-BIC.

For the practical implementation of such structures, it should be possible to use several methods specially developed for obtaining hybrid Janus particles of various shapes [23,59,60]. We suggest the following possible fabrication workflow: First, dry etching creates equidistant strips on the silicon substrate with a depth of 200 nm and a period equal to the structure's period [61]. Gold is then deposited into the hollow areas, forming alternating gold and silicon strips. Finally, reactive-ion etching through a mask [1] refines the structure to create a metasurface of hybrid cylinder-shaped particles.

ACKNOWLEDGMENTS

M.A.P. and C.R. acknowledge support through the Deutsche Forschungsgemeinschaft (DFG, German Research Foundation) under Germany's Excellence Strategy via the Excellence Cluster 3D Matter Made to Order (EXC-2082/1, Grant No. 390761711) and from the Carl Zeiss Foundation via CZF-Focus@HEiKA. M.A.P. acknowledges support within Erasmus+ program and from region Bourgogne Franche-Comté, France. A.B.E. acknowledges support of the Deutsche Forschungsgemeinschaft (DFG, German Research Foundation) under Germanys Excellence Strategy within the Cluster of Excellence PhoenixD (EXC2122, Project ID No. 390833453).

DATA AVAILABILITY

The data that support the findings of this article are not publicly available upon publication because it is not technically feasible and/or the cost of preparing, depositing, and hosting the data would be prohibitive within the terms of this research project. The data are available from the authors upon reasonable request.

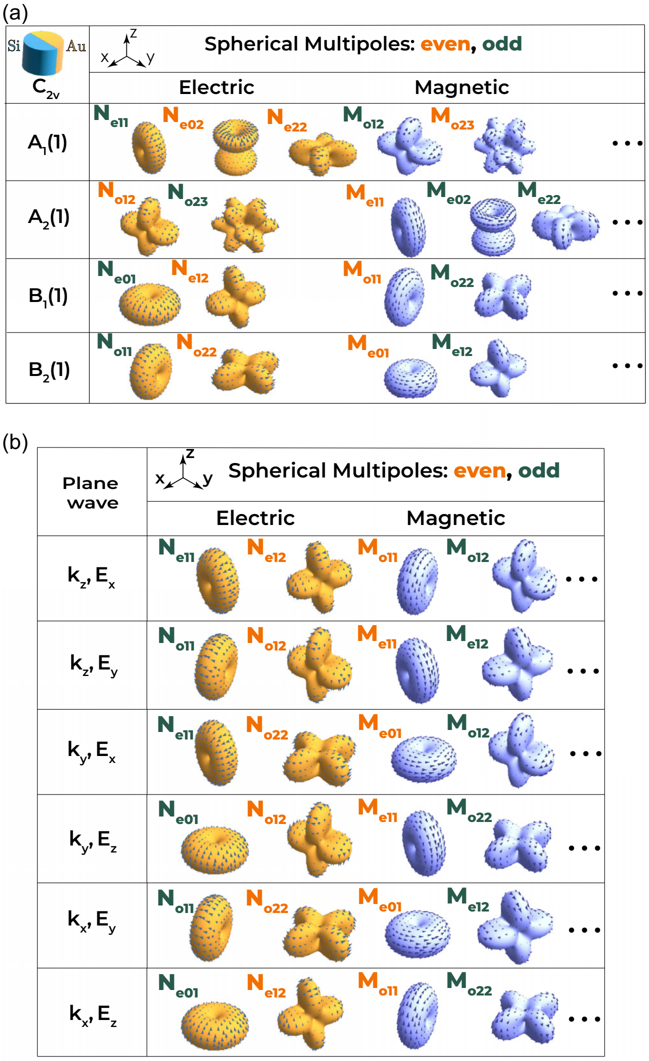

FIG. 10. (a) The multipolar decomposition into VSHs of the eigenmodes of a particle with the symmetry group C_{2v}. (b) Decomposition into VSHs of plane waves with all configurations. The blue VSHs represent the magnetic harmonics, while the yellow ones the electric harmonics. The shape of the figure depicts the far-field radiation pattern of each multipole, the arrows correspond to the field polarization.

APPENDIX A: DEFINITION OF VECTOR SPHERICAL HARMONICS

The vector spherical harmonics are defined in the following way,

$$\begin{aligned}\mathbf{M}_{(e,o)m\ell} &= \nabla \times (\mathbf{r}\psi_{(e,o)m\ell})\\ \mathbf{N}_{(e,o)m\ell} &= \frac{\nabla \times \mathbf{M}_{(e,o)m\ell}}{k},\end{aligned} \tag{A1}$$

where

$$\psi_{em\ell}(kr) = P_\ell^m(\cos\theta)z_\ell(kr)\cos m\varphi$$
$$\psi_{om\ell}(kr) = P_\ell^m(\cos\theta)z_\ell(kr)\sin m\varphi. \tag{A2}$$

Here, $\psi_{(e,o)m\ell}(kr)$ are the solutions of the scalar Helmholtz equation with the wave vector k, $P_\ell^m(\cos\theta)$ is associated Legendre polynomial, $z_\ell(kr)$ is any of the four spherical Bessel functions, m is an integer, and $m \geqslant 0$.

APPENDIX B: TABLES

The decomposition of the eigenmodes into VSHs of the hybrid cylinder is collected in the Table presented in Fig. 10(a). The decomposition into VSHs of all configurations of plane waves is presented in Fig. 10(b) [51].

[1] D. G. Baranov, D. A. Zuev, S. I. Lepeshov, O. V. Kotov, A. E. Krasnok, A. B. Evlyukhin, and B. N. Chichkov, All-dielectric nanophotonics: The quest for better materials and fabrication techniques, Optica **4**, 814 (2017).

[2] M. Pelton, J. Aizpurua, and G. Bryant, Metal-nanoparticle plasmonics, Laser Photonics Rev. **2**, 136 (2008).

[3] V. Giannini, A. I. Fernández-Domínguez, S. C. Heck, and S. A. Maier, Plasmonic nanoantennas: Fundamentals and their use in controlling the radiative properties of nanoemitters, Chem. Rev. **111**, 3888 (2011).

[4] W. Li and J. Valentine, Metamaterial perfect absorber based hot electron photodetection, Nano Lett. **14**, 3510 (2014).

[5] J. Wang, A. Coillet, O. Demichel, Z. Wang, D. Rego, A. Bouhelier, P. Grelu, and B. Cluzel, Saturable plasmonic metasurfaces for laser mode locking, Light: Sci. Appl. **9**, 50 (2020).

[6] A. K. Azad, W. J. Kort-Kamp, M. Sykora, N. R. Weisse-Bernstein, T. S. Luk, A. J. Taylor, D. A. Dalvit, and H.-T. Chen, Metasurface broadband solar absorber, Sci. Rep. **6**, 20347 (2016).

[7] G. Baffou, F. Cichos, and R. Quidant, Applications and challenges of thermoplasmonics, Nat. Mater. **19**, 946 (2020).

[8] V. E. Babicheva and A. B. Evlyukhin, Mie-resonant metaphotonics, Adv. Opt. Photonics **16**, 539 (2024).

[9] K. Koshelev and Y. Kivshar, Dielectric resonant metaphotonics, ACS Photonics **8**, 102 (2021).

[10] A. I. Kuznetsov, A. E. Miroshnichenko, M. L. Brongersma, Y. S. Kivshar, and B. Luk'yanchuk, Optically resonant dielectric nanostructures, Science **354**, aag2472 (2016).

[11] A. B. Evlyukhin, C. Reinhardt, A. Seidel, B. S. Luk'yanchuk, and B. N. Chichkov, Optical response features of Si-nanoparticle arrays, Phys. Rev. B **82**, 045404 (2010).

[12] A. García-Etxarri, R. Gómez-Medina, L. S. Froufe-Pérez, C. López, L. Chantada, F. Scheffold, J. Aizpurua, M. Nieto-Vesperinas, and J. J. Sáenz, Strong magnetic response of submicron silicon particles in the infrared, Opt. Express **19**, 4815 (2011).

[13] A. B. Evlyukhin, S. M. Novikov, U. Zywietz, R. L. Eriksen, C. Reinhardt, S. I. Bozhevolnyi, and B. N. Chichkov, Demonstration of magnetic dipole resonances of dielectric nanospheres in the visible region, Nano Lett. **12**, 3749 (2012).

[14] A. I. Kuznetsov, A. E. Miroshnichenko, Y. H. Fu, J. Zhang, and B. Luk'yanchuk, Magnetic light, Sci. Rep. **2**, 492 (2012).

[15] M. R. Shcherbakov, D. N. Neshev, B. Hopkins, A. S. Shorokhov, I. Staude, E. V. Melik-Gaykazyan, M. Decker, A. A. Ezhov, A. E. Miroshnichenko, I. Brener *et al.*, Enhanced third-harmonic generation in silicon nanoparticles driven by magnetic response, Nano Lett. **14**, 6488 (2014).

[16] K. V. Baryshnikova, A. Novitsky, A. B. Evlyukhin, and A. S. Shalin, Magnetic field concentration with coaxial silicon nanocylinders in the optical spectral range, J. Opt. Soc. Am. B **34**, D36 (2017).

[17] A. Krasnok, M. Caldarola, N. Bonod, and A. Alú, Spectroscopy and biosensing with optically resonant dielectric nanostructures, Adv. Opt. Mater. **6**, 1701094 (2018).

[18] A. B. Evlyukhin, C. Reinhardt, and B. N. Chichkov, Multipole light scattering by nonspherical nanoparticles in the discrete dipole approximation, Phys. Rev. B **84**, 235429 (2011).

[19] I. Staude, A. E. Miroshnichenko, M. Decker, N. T. Fofang, S. Liu, E. Gonzales, J. Dominguez, T. S. Luk, D. N. Neshev, I. Brener, and Y. Kivshar, Tailoring directional scattering through magnetic and electric resonances in subwavelength silicon nanodisks, ACS Nano **7**, 7824 (2013).

[20] P. D. Terekhov, K. V. Baryshnikova, Y. A. Artemyev, A. Karabchevsky, A. S. Shalin, and A. B. Evlyukhin, Multipolar response of nonspherical silicon nanoparticles in the visible and near-infrared spectral ranges, Phys. Rev. B **96**, 035443 (2017).

[21] D. Ray, A. Kiselev, and O. J. F. Martin, Multipolar scattering analysis of hybrid metal-dielectric nanostructures, Opt. Express **29**, 24056 (2021).

[22] X. Han, K. Liu, and C. Sun, Plasmonics for biosensing, Materials **12**, 1411 (2019).

[23] Á. Barreda, F. Vitale, A. E. Minovich, C. Ronning, and I. Staude, Applications of hybrid metal-dielectric nanostructures: State of the art, Adv. Photonics Res. **3**, 2100286 (2022).

[24] S. I. Lepeshov, A. E. Krasnok, P. A. Belov, and A. E. Miroshnichenko, Hybrid nanophotonics, Phys. -Usp. **61**, 1035 (2019).

[25] D. Ray, T. V. Raziman, C. Santschi, D. Etezadi, H. Altug, and O. J. F. Martin, Hybrid metal-dielectric metasurfaces for refractive index sensing, Nano Lett. **20**, 8752 (2020).

[26] S. Abdollahramezani, O. Hemmatyar, M. Taghinejad, H. Taghinejad, Y. Kiarashinejad, M. Zandehshahvar, T. Fan, S. Deshmukh, A. A. Eftekhar, W. Cai *et al.*, Dynamic hybrid metasurfaces, Nano Lett. **21**, 1238 (2021).

[27] R. Guo, E. Rusak, I. Staude, J. Dominguez, M. Decker, C. Rockstuhl, I. Brener, D. N. Neshev, and Y. S. Kivshar, Multipolar coupling in hybrid metal–dielectric metasurfaces, ACS Photonics **3**, 349 (2016).

[28] C. P. T. McPolin, Y. N. Vila, A. V. Krasavin, J. Llorca, and A. V. Zayats, Multimode hybrid gold-silicon nanoantennas for tailored nanoscale optical confinement, Nanophotonics **12**, 2997 (2023).

[29] J. Wohlwend, A. Hilti, C. Polinari, R. Spolenak, and H. Galinski, Hybrid resonant metasurfaces with configurable structural colors, Adv. Opt. Mater. **12**, 2401501 (2024).

[30] Y. Chen, Y. Zhang, and A. F. Koenderink, General point dipole theory for periodic metasurfaces: Magnetoelectric scattering lattices coupled to planar photonic structures, Opt. Express **25**, 21358 (2017).

[31] A. Kodigala, T. Lepetit, Q. Gu, B. Bahari, Y. Fainman, and B. Kanté, Lasing action from photonic bound states in continuum, Nature (London) **541**, 196 (2017).

[32] V. R. Tuz, V. V. Khardikov, A. S. Kupriianov, K. L. Domina, S. Xu, H. Wang, and H.-B. Sun, High-quality trapped modes in all-dielectric metamaterials, Opt. Express **26**, 2905 (2018).

[33] K. Koshelev, S. Lepeshov, M. Liu, A. Bogdanov, and Y. Kivshar, Asymmetric metasurfaces with high-Q resonances governed by bound states in the continuum, Phys. Rev. Lett. **121**, 193903 (2018).

[34] A. Sayanskiy, A. S. Kupriianov, S. Xu, P. Kapitanova, V. Dmitriev, V. V. Khardikov, and V. R. Tuz, Controlling high-Q trapped modes in polarization-insensitive all-dielectric metasurfaces, Phys. Rev. B **99**, 085306 (2019).

[35] S. Li, C. Zhou, T. Liu, and S. Xiao, Symmetry-protected bound states in the continuum supported by all-dielectric metasurfaces, Phys. Rev. A **100**, 063803 (2019).

[36] A. S. Kupriianov, Y. Xu, A. Sayanskiy, V. Dmitriev, Y. S. Kivshar, and V. R. Tuz, Metasurface engineering through bound states in the continuum, Phys. Rev. Appl. **12**, 014024 (2019).

[37] A. B. Evlyukhin, M. A. Poleva, A. V. Prokhorov, K. V. Baryshnikova, A. E. Miroshnichenko, and B. N. Chichkov, Polarization switching between electric and magnetic quasi-trapped modes in bianisotropic all-dielectric metasurfaces, Laser Photonics Rev. **15**, 2100206 (2021).

[38] A. B. Evlyukhin, V. R. Tuz, V. S. Volkov, and B. N. Chichkov, Bianisotropy for light trapping in all-dielectric metasurfaces, Phys. Rev. B **101**, 205415 (2020).

[39] S. I. Azzam and A. V. Kildishev, Photonic bound states in the continuum: From basics to applications, Adv. Opt. Mater. **9**, 2001469 (2021).

[40] S. A. Schulz, R. Oulton, M. Kenney, A. Alù, I. Staude, A. Bashiri, Z. Fedorova, R. Kolkowski, A. F. Koenderink, X. Xiao *et al.*, Roadmap on photonic metasurfaces, Appl. Phys. Lett. **124**, 260701 (2024).

[41] A. I. Kuznetsov, M. L. Brongersma, J. Yao, M. K. Chen, U. Levy, D. P. Tsai, N. I. Zheludev, A. Faraon, A. Arbabi, N. Yu *et al.*, Roadmap for optical metasurfaces, ACS Photonics **11**, 816 (2024).

[42] M. A. Green, Self-consistent optical parameters of intrinsic silicon at 300 K including temperature coefficients, Sol. Energy Mater. Sol. Cells **92**, 1305 (2008).

[43] P. B. Johnson and R. W. Christy, Optical constants of the noble metals, Phys. Rev. B **6**, 4370 (1972).

[44] A. B. Evlyukhin and B. N. Chichkov, Multipole decompositions for directional light scattering, Phys. Rev. B **100**, 125415 (2019).

[45] J. D. Jackson, *Classical Electrodynamics*, 3rd ed. (John Wiley & Sons. Inc., New York, 1999)

[46] R. Alaee, C. Rockstuhl, and I. Fernandez-Corbaton, An electromagnetic multipole expansion beyond the long-wavelength approximation, Opt. Commun. **407**, 17 (2018).

[47] P. D. Terekhov, V. E. Babicheva, K. V. Baryshnikova, A. S. Shalin, A. Karabchevsky, and A. B. Evlyukhin, Multipole analysis of dielectric metasurfaces composed of nonspherical nanoparticles and lattice invisibility effect, Phys. Rev. B **99**, 045424 (2019).

[48] I. Allayarov, A. B. Evlyukhin, and A. Calà Lesina, Multiresonant all-dielectric metasurfaces based on high-order multipole coupling in the visible, Opt. Express **32**, 5641 (2024).

[49] Z. Xiong, Q. Yang, W. Chen, Z. Wang, J. Xu, W. Liu, and Y. Chen, On the constraints of electromagnetic multipoles for symmetric scatterers: Eigenmode analysis, Opt. Express **28**, 3073 (2020).

[50] S. Gladyshev, K. Frizyuk, and A. Bogdanov, Symmetry analysis and multipole classification of eigenmodes in electromagnetic resonators for engineering their optical properties, Phys. Rev. B **102**, 075103 (2020).

[51] M. Poleva, K. Frizyuk, K. Baryshnikova, A. Evlyukhin, M. Petrov, and A. Bogdanov, Multipolar theory of bianisotropic response of meta-atoms, Phys. Rev. B **107**, L041304 (2023).

[52] K. Achouri and O. J. F. Martin, Extension of Lorentz reciprocity and Poynting theorems for spatially dispersive media with quadrupolar responses, Phys. Rev. B **104**, 165426 (2021).

[53] V. S. Asadchy, I. A. Faniayeu, Y. Radi, and S. A. Tretyakov, Determining polarizability tensors for an arbitrary small electromagnetic scatterer, Photonics Nanostruct. Fundam. Appl. **12**, 298 (2014).

[54] M. Yazdi and N. Komjani, Polarizability calculation of arbitrary individual scatterers, scatterers in arrays, and substrated scatterers, J. Opt. Soc. Am. B **33**, 491 (2016).

[55] A. Kwadrin and A. F. Koenderink, Probing the electrodynamic local density of states with magnetoelectric point scatterers, Phys. Rev. B **87**, 125123 (2013).

[56] I. Sersic, C. Tuambilangana, T. Kampfrath, and A. F. Koenderink, Magnetoelectric point scattering theory for metamaterial scatterers, Phys. Rev. B **83**, 245102 (2011).

[57] V. G. Kravets, A. V. Kabashin, W. L. Barnes, and A. N. Grigorenko, Plasmonic surface lattice resonances: A review of properties and applications, Chem. Rev. **118**, 5912 (2018).

[58] V. E. Babicheva and A. B. Evlyukhin, Multipole lattice effects in high refractive index metasurfaces, J. Appl. Phys. **129**, 040902 (2021).

[59] J. Hu, S. Zhou, Y. Sun, X. Fang, and L. Wu, Fabrication, properties and applications of Janus particles, Chem. Soc. Rev. **41**, 4356 (2012).

[60] X. Pang, C. Wan, M. Wang, and Z. Lin, Strictly biphasic soft and hard Janus structures: Synthesis, properties, and applications, Angew. Chem., Int. Ed. **53**, 5524 (2014).

[61] P.-S. Yang, P.-H. Cheng, C. R. Kao, and M.-J. Chen, Novel self-shrinking mask for sub-3 nm pattern fabrication, Sci. Rep. **6**, 1 (2016).